Tuning the nanoporous structure of carbons derived from composite of cross-linked polymers for charge storage applications

Farshad Barzegar[*,1], Vladimir Pavlenko[2], Muhammad Zahid[3], Abdulhakeem Bello[4,5], Xiaohua Xia[1], Ncholu Manyala[5], Kenneth I. Ozoemena[6], Qamar Abbas*[*,7]*

[1] Electrical, Electronic and Computer Engineering Department, University of Pretoria, Pretoria 0002, South Africa

[2] Al-Farabi Kazakh National University, 71 al-Farabi Ave., 050040 Almaty, Kazakhstan

[3] Department of Chemistry, University of Agriculture, 38000 Faisalabad, Pakistan

[4] Department of Theoretical and Applied Physics, African University of Science and Technology, Km. 10 Airport Road, Galadimawa, Abuja, Nigeria

[5] Department of Physics, University of Pretoria, Pretoria 0002, South Africa

[6] School of Chemistry, Molecular Science Institute, University of the Witwatersrand, Private Bag 3, P O Wits, Johannesburg 2050, South Africa

[7] Institute for Chemistry and Technology of Materials, Graz University of Technology, Stremayrgasse 9, 8010 Graz, Austria

Email of corresponding authors: qamar.abbas@tugraz.at ; farshadbarzegar@gmail.com

TABLE OF CONTENT

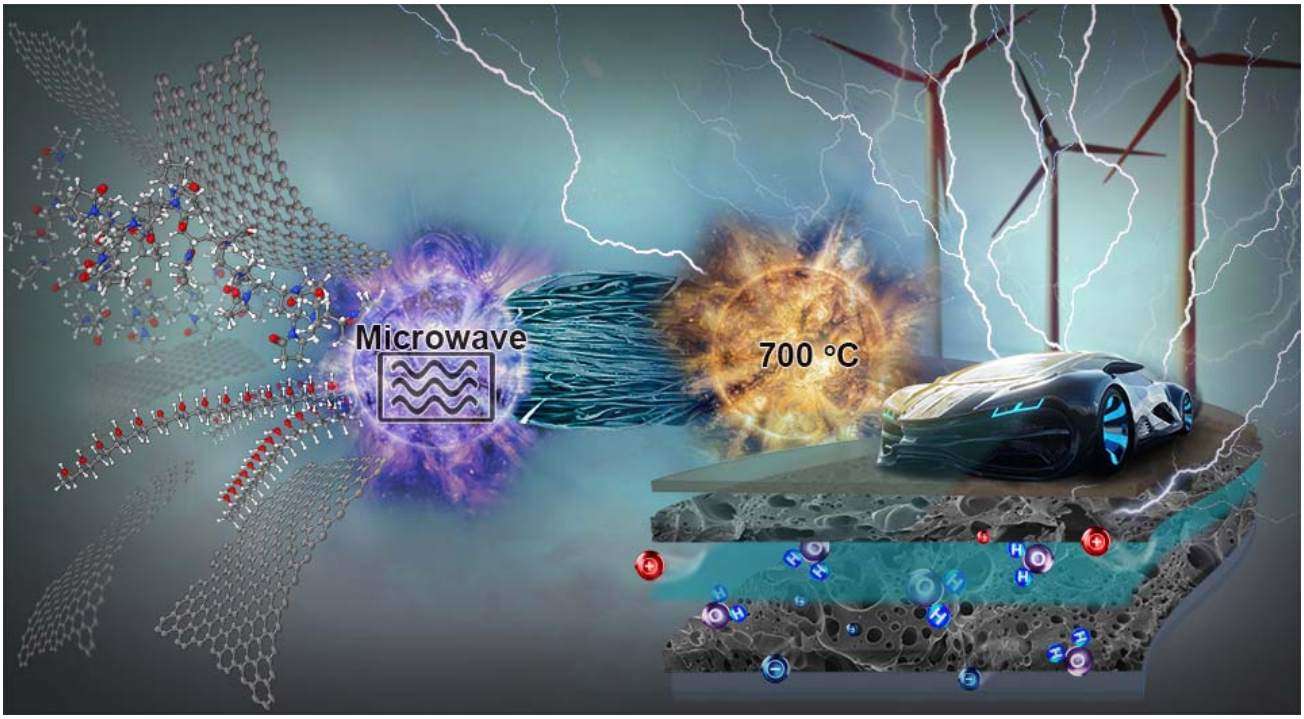

ABSTRACT

Controlling the porosity of carbon-based electrodes is key towards performance improvement of charge storage devices e.g., supercapacitors, which deliver high power via fast charge/discharge of ions at the electrical double-layer (EDL). Here, eco-friendly preparation of carbons with adaptable nanopores from polymers obtained via microwave-assisted cross-linking of polyvinyl alcohol (PVA) and polyvinyl pyrrolidone (PVP) is reported. The polymeric hydrogels possess porous and foam-like structures giving an excellent control of porosity at the precursor level, which are then subjected to activation at high temperatures 700-900 °C to prepare carbons with a surface area up to 1846 $m^2 g^{-1}$ and uniform distribution of micro-, meso- and macro-pores. Then, graphene as an additive to hydrogel improves the surface characteristics and elaborates porous texture, giving composite materials with a surface area of 3107 $m^2 g^{-1}$. These carbons show interconnected

porous structure and bi-modal pore size distribution suitable for facile ionic transport. When implemented in symmetric supercapacitor configuration with aqueous 5 mol L^{-1} $NaNO_3$ electrolyte, a capacitance of 163 F g^{-1} (per average mass of one electrode) and stable evolution of capacitance, coulombic, and energy efficiency during 10,000 galvanostatic charge/discharge up to 1.6 V at 1.0 A g^{-1} has been achieved.

KEYWORDS: Microwave-assisted cross-linked polymers; nanoporous carbon; charge storage; electric double-layer; supercapacitor

INTRODUCTION

To meet the increasing energy demand of the modern world and to fill the niches requiring fast energy delivery and its simultaneous quick recovery,[1-5] new materials and methods are desirable. Carbon materials make up to 90 wt.% of the electrode composition used in capacitive charge storage technologies such as supercapacitors are attractive devices for capturing energy from regenerative braking in tramways or in a start-stop system for automobiles.[6-8] Commercial carbons are mainly derived from biomass sources with pre-defined natural structure,[9-11] thus restricting the control over efficient storing and releasing of charges and hence their viability in ever-growing energy sector. New methods and materials for designing carbons with optimized and compatible pore structure which can be tuned per application, is therefore highly desirable. Since the fast charging/discharging of electric double-layer (EDL) depends on the respective size of ions and pores,[12] this compatibility is at the heart of high power and long-term cycling of supercapacitors.

Eliad et al. have shown that the molecular sieving effect appears when the size of ions approaches the pore size of carbon. For example, in the case of aqueous magnesium sulfate electrolyte, where

the size of hydrated ions (Mg^{2+} and SO_4^{2-}) is larger than the average pore size of carbon (0.51 nm), less capacitive current is obtained.[13-14] In this respect, one could infer that maximum capacitance can be achieved with a large number of ions fitting to the pores and by this way taking full advantage of ion versus pore compatibility aspect.[15] Leaving aside the discussion related with nitrogen as a probe for estimating surface and pore sizes, one would still argue over the importance of pore and ion size compatibility, which is further evidenced when ionic liquids are used as electrolytes for charge storage in nanoporous carbons.[16-17] More importantly, it has been found that the majority of pores of carbon are underused due to their small size compared to the effective size of ions as well as their orientation while entering the pore.[18]

From the foregoing, it is clear that pore tuning in carbon materials is an essential parameter, and efforts in this direction have yielded little progress so far. Indeed, high temperature and pressure treatment of a zeolite template carbon resulted in reduced average micropore size, however, similar changes in density and pore texture were not observed for commercial carbons.[19] Templated carbons, on the other hand, give control of microporous structure and pore interconnectivity in carbon owing to the structural regularity possessed by the incorporated template materials.[20-22] However, high synthesis cost and the use of aggressive acids such as HF to remove the template materials hinder the viability of this method.

This work presents a new strategy to control the porosity of carbons by firstly obtaining a precursor with highly refined pores, setting the guideline for the porosity of final carbon product. In addition to other advantages, producing hydrogels from cross-linked polymers is environmentally friendly, non-toxic, and cheap. Cross-linked porous polymers offer a great opportunity to control porous structure, surface area, and adsorption properties.[23-24] As a result of the controlled porosity at different length scales, such materials possess interconnected pore structure that facilitates the

diffusion of ions and molecules.[25] Previously, polymer-based precursors have been carbonized and activated to prepare carbons and some of them have been efficiently used for charge storage application.[26-30] However, no systematic porous texture was studied owing to the absence of pre-defined precursor's structural footprints. Here, we show the use of cross-linked polymer-based precursor to obtain carbons with a wide range of pore diameter fitting the size of the maximum number of ions and efficiently charging the EDL **(Figure 1)**, and then preparing composites with graphene to further improve the charge storage capability of these carbons.[31-33]

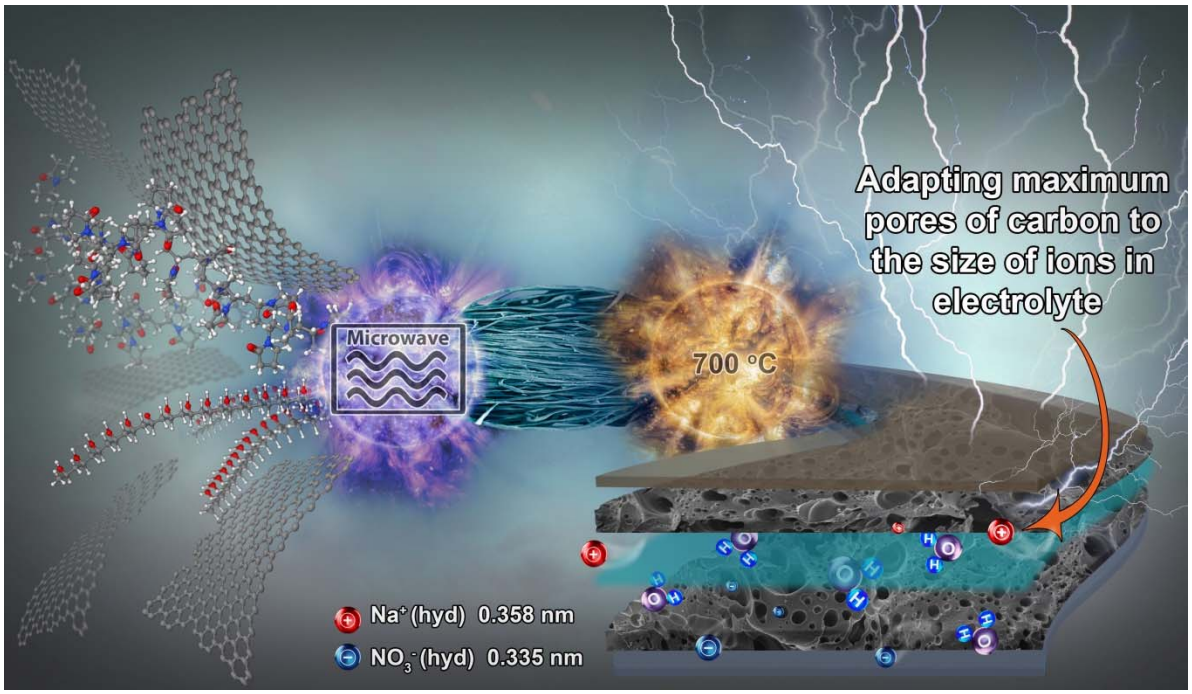

Figure 1. Cross-linking of polymers and formation of hydrogel via microwave irradiation. The porous hydrogel is then subjected to carbonization and activation at high temperature to prepare nanoporous carbons with majority of pores adaptable for ionic transport and to gain maximum charge storage.

EXPERIMENTAL SECTION

Preparation of nanoporous carbons

An aqueous solution of polyvinyl alcohol (PVA) was prepared at a concentration of 10 wt.% and then polyvinyl pyrrolidone (PVP) was added to the solution while gradually increasing its mass ratio to PVA. Hydrochloric acid (37%) was added at a volume ratio of 1.5:100 to the aqueous mixture of PVA and PVP as the cross-linking agent.[34]. The molecular weight of used PVA and PVP are 89000-98000 and 10000 respectively. The mixtures were sonicated for 30 minutes and then stirred using magnetic stirring for another 30 min at room temperature to obtain a respective homogeneous dispersion. Each solution with fully dispersed components was then transferred to a microwave reactor (Anton Paar Synthos 3000 multimode reactor) at 1400 W magnetron power, equipped with a wireless pressure and temperature sensor. The reactor was operated in the pressure mode using a power of 500 W; the sample temperature was ramped at 10°C/min up to 190°C and kept at this temperature for different reaction times. The schematic diagram for the preparation process of activated carbons is shown in Figure S1 (in *supporting information*). For the second type of sample, lab-scale prepared graphene by chemical vapor deposition (CVD) [35] was introduced to the initial mixture of PVP and PVA (4:6). and all composition was subjected to microwave irradiation. The cross-linked hydrogel material exhibited a consistent structure with or without graphene incorporated into it. The composites without graphene were first activated with KOH at 700°C, 800°C, and 900°C to select a suitable activation temperature. Afterward, the PVP: PVA hydrogels with and without graphene were carbonized and activated at 700°C (best activation temperature). The obtained carbon materials after the activation process were further cleaned with diluted hydrochloric acid and then dried at 120°C for 12 hours to remove water contents before further physicochemical investigations. To compare the surface area, 10 wt.% PVP was also

carbonized and activated at 700°C, 800°C, and 900°C, and obtained carbon materials were washed and cleaned in a similar fashion as mentioned previously. For the electrochemical investigations, the selected samples were post-treated at 700°C for 1 hour under nitrogen atmosphere to remove any remaining oxygenated functional groups from the surface of carbons.

Structural characterization of nanoporous carbons

Nitrogen adsorption-desorption isotherms were measured at −196°C using a Micromeritics ASAP 2020. Before analysis, samples (80 mg each) were degassed at 140°C for 12 hours under vacuum. The surface area was calculated by the Brunauer–Emmett–Teller (BET) method from the adsorption branch in the relative pressure range (P/P_0) of 0.01 - 0.2. Selected samples were also characterized using powder X-ray diffraction (XRD) employing an XPERT-PRO diffractometer (PANalytical BV, Netherlands) with theta/theta geometry, operating a cobalt tube at 35 kV and 50 mA. The XRD patterns of all specimens were recorded in the 10.0° – 80.0° 2θ range with a counting time of 5.240 seconds per step. The SEM images were obtained on a Zeiss Ultra Plus 55 field emission scanning electron microscope (FE-SEM) operated at an accelerating voltage of 2.0 kV. Raman spectroscopic analysis of the graphene and composite materials was performed using a T64000 micro-Raman spectrometer from HORIBA Scientific, Jobin Yvon Technology equipped with a triple monochromator system to eliminate contributions from the Rayleigh line. All the samples were analyzed with a 514 nm argon excitation laser with a power of 12 mW at laser exit to avoid thermal effects. Thermogravimetric Analysis (TGA) was carried out using TA Instruments Q600 Simultaneous DSC/TG which measures the weight change in a material as a function of temperature or time under a controlled atmosphere. TGA samples were heated from room temperature to 1000°C at a rate of 10°C min^{-1}.

Electrodes preparation and electrochemical investigation of supercapacitors

For the preparation of electrodes, a mixture of active carbon materials 90 wt.%, polytetrafluoroethylene (PTFE) binder 5 wt.% (from Sigma-Aldrich) and conductivity additive 5 wt.% (SUPER C65 from TIMCAL) were homogenized and dispersed in pure ethanol, and the slurry was then uniformly rolled to prepare the electrode sheet. The electrodes were pasted on to the current collector and dried at 100°C in an oven for 12 hours to ensure complete evaporation of ethanol and adsorbed water. The electrochemical test of the symmetric cell was carried out in a two-electrode cell configuration using Swagelok-type cells with a mass loading of ~5.0 mg for each electrode with a thickness of 0.15 mm and a diameter of 8.0 mm, using a glass microfiber filter paper as the separator soaked with 5 mol L^{-1} $NaNO_3$ aqueous electrolyte solution. Electrochemical measurements were carried out (on SP-300 potentiostat from Bio-Logic) such as cyclic voltammetry (CV), galvanostatic charge/discharge (GCPL), and electrochemical impedance spectroscopy (EIS) up to various voltages. The CV tests were carried out in the potential range of 0 to 1.6 V at different scan rates ranging from 2 mV s^{-1} to 200 mV s^{-1}, GCPL from 0.2 A g^{-1} to 5 A g^{-1} and electrochemical impedance spectroscopy (EIS) measurements were conducted in the frequency range from 1 mHz to 100 kHz at open circuit voltage (OCV), 0.8 V, 1.0 V, 1.2 V, 1.4 V and 1.6 V.

The galvanostatic charge-discharge tests based on the two-electrode cell was used for the evaluation of the specific capacitance (C_{sp}: F g^{-1}), The area capacitances (C_{area}: F cm^{-2}), the area energy density (E_a: Wh cm^{-2}), and the area power density of the cell (P_a: kW cm^{-2}) was calculated respectively using equations 1 to 3 given below. Generally, the full capacitance (CF) of a supercapacitor device is the manifestation of the electrical charge ΔQ stored at a given voltage change ΔV and can be written as supercapacitors performance evaluation:[36-37]

$$C = \frac{I\Delta t}{\Delta V} \tag{1}$$

Nonetheless, the intrinsic specific capacitance of a single electrode in a symmetric cell is the preferred parameter, and it estimates the charge storage capability of electrode materials and is expressed as:

$$C_{sp} = \frac{4C}{m} \tag{2}$$

$$C_{sa} = \frac{C}{SA} \tag{3}$$

where C_{sp} (F g^{-1}) is the specific capacitance, C_{sa} is the capacitance per SA, I (A) is the charge/discharge current, ΔV (V) stands for the potential window within the discharge time Δt (s), m (g) corresponds to the amount of active material on the electrode and SA is the surface area of the electrodes

The corresponding specific energy, areal energy, specific power and areal power for the symmetric cell are calculated according to equations 4 and 7 respectively:

$$E_{\max} = \frac{1}{2}C\left(\Delta V\right)^2 = \frac{1000 \times C_{sp} \times \Delta V^2}{2 \times 4 \times 3600} = \frac{C_{sp} \times \Delta V^2}{28.8} \tag{4}$$

$$E_{areal} = \frac{1}{2}C\left(\Delta V\right)^2 = \frac{C_{sa} \times \Delta V^2}{2 \times 4 \times 3600 \times A} \tag{5}$$

$$P_{\max} = \frac{3.6 \times E_{\max}}{\Delta t} \tag{6}$$

$$P_{areal} = \frac{3.6 \times E_{areal}}{\Delta t} \tag{7}$$

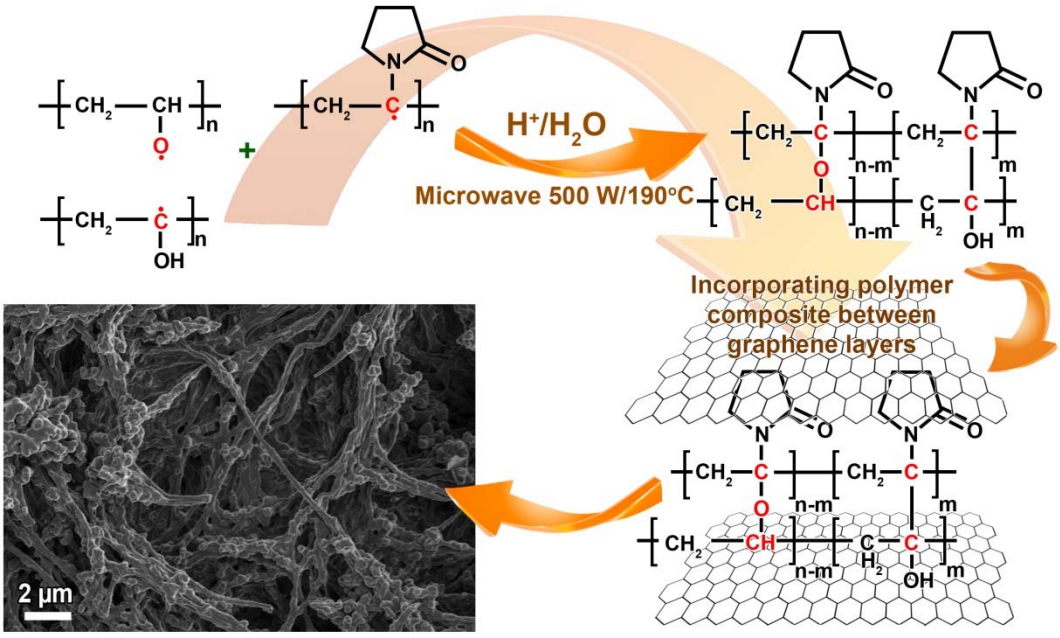

Figure 2. Reaction between PVP and PVA assisted by the microwave irradiation to form polymer hydrogel with and without graphene addition. The two composite materials are then processed through chemical activation. The addition of graphene facilitates in maintaining the porous structure and prevents from structural collapse of interlayer spacing.

RESULTS AND DISCUSSION

Synthesis and characterization of cross-linked polymers based carbons

At the first step, a reduction reaction between PVA and PVP polymers was carried out to produce hydrogels via a simple microwave-assisted technique. Production of the hydrogel by cross-linking of PVA and PVP is well-known in the literature,[31-33] however, the use of microwave has been rarely attempted. The microwave irradiation helps to create radical sites at the -OH groups of PVA and/or at the main carbon chain of polymer which participate in cross-linking via hydrogen bonding **(Figure 2)**. For the second part, an aqueous suspension of PVA and PVP were prepared with graphene as an additive and the mixture was subjected to microwave treatment. The same reaction mechanism follows the generation of radical and hydrogel incorporated with graphene

was obtained which was ready to be subjected to carbonization and activation. The activation was performed by KOH where alkali and the composite material mass ratio of 1:3 was maintained. The activation was performed at three temperatures i.e., 700°C, 800°C, and 900°C to select the most effective value with regard to carbon characteristics and performance parameters.

The internal three-dimensional networks observed for the hydrogel sample in **Figure 3a** show the high connectivity of fibers and the presence of preliminary pores in the polymer structure. The hydrogel material under the activation and carbonization conditions transformed into an excessive network of channels and evolving new pore structures. The creation of such channels is expected owing to the release of gases (CO, H_2O, and CO_2) which are formed initially during the carbonization stage and then the chemical activation.[38-39] With an increase of PVP ratio, the transport channels were clearly visible and the large pores appeared on the surface **(Figure 3b-f)**. These big channels or network of pores leads to smaller pores within the carbon matrix providing facile access to the bulk carbon material. Overall, the development of pore structure is progressive in nature owing to the increasing fraction of PVP to the PVA solution which improves the pore morphology at the hydrogel precursor level (Figure S2 in *supporting information*). Thanks to the initial pore structure of the hydrogel formed by the reaction of PVA and PVP, general wide surfaced sheet-like structures are observed after the activation with the different percentages of PVP from ratio 1:9 to 4:6 as seen in SEM images. A further increase of PVP ratio to 5:5 (Figure 3f) results in a totally different structure of hydrogel which has a more solid form and is unsuitable for preparing porous carbon.

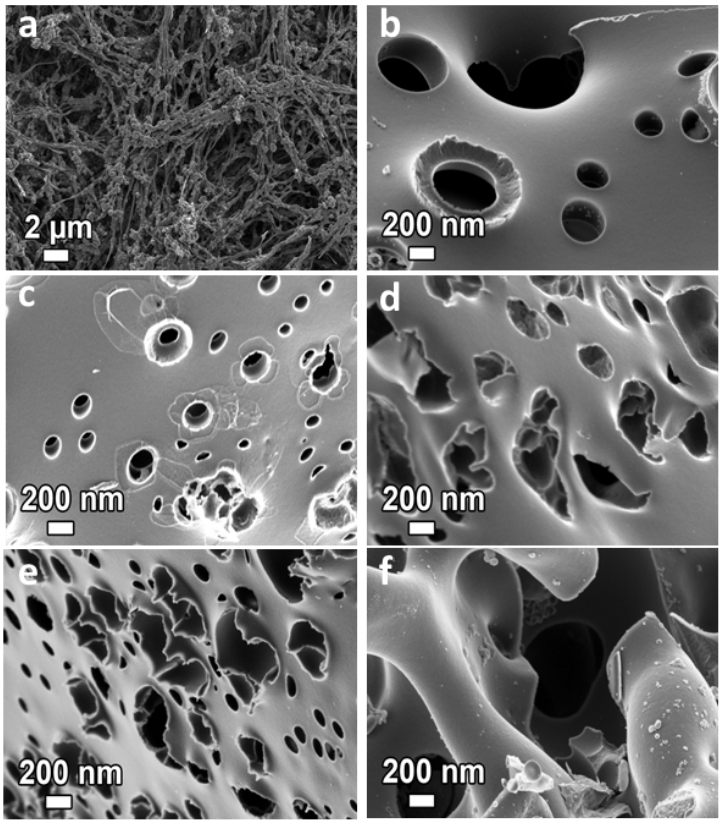

Figure 3. (a) SEM images of PVP:PVA hydrogel before activation and carbonization, then gradual increase of PVP to PVA ratio and after activation (b) 1:9, (c) 2:8, (d) 3:7, (e) 4:6, (f) 5:5.

Nitrogen gas adsorption isotherms for the carbons obtained by the activation of PVA (10 wt.%) alone at a different temperature to find the best sample preparation condition are presented in Figure S3. The sample obtained at 700°C has the highest BET surface area **(Table 1)** and possesses a high number of small pores (0.204 cm^3 g^{-1} micropore volume for a total pore volume of 0.307 cm^3 g^{-1}). The shape of adsorption/desorption isotherm also suggests the presence of mainly micropores and the reversibility is a direct indication of good pore connectivity and the presence of adjacent channels. Further enhancing the activation temperature to 800°C and 900°C causes the reduction of surface area and blockage of pores indicated by the sharp rise of isotherm at high-pressure region. Activation by chemicals at a higher temperature may block access to micropores

which is also indicated by decreased surface area.[40-41] Hence, for preparing further carbon materials in this work, an activation temperature of 700°C was selected. To obtain carbons with appropriate and well-organized pore structure, hydrogel samples with the varying percentages of PVP were subjected to carbonization and activation. This method was also helpful to obtain the optimum ratio of PVA to PVP and its effect on the surface area of the resulting activated carbon were investigated. The first four carbon samples (from 1:9 to 4:6) with increasing fraction of PVP show the reversible Type I isotherm **(Figure 4a-c and Figure S4a)**, which is normally associated with microporous solids having relatively small external surfaces. Their limiting uptake of nitrogen is generally governed by the accessible micropore volume rather than by the surface area. Hence, a large number of the surface area is represented by the high micropore volume and presence of interconnected pores.

Table 1. BET surface area versus carbonization temperature of PVA (10 wt.%) sample.

T_C [a)]	700°C	800°C	900°C
BET ($m^2\ g^{-1}$)	537	449	85

[a)] temperature at which PVA is carbonized and activated.

The sample with PVA to PVP ratio 5:5 shows a deviation of the adsorption and desorption curves from the previous trend **(Figure 4d)**. Although such an isotherm could feature the Type H3 loop which is generally associated with monolayer coverage and the start of multilayer sorption on nonporous materials. In this case, however, it indicates the Type I isotherm, characteristic for the presence of micropores in the carbon material together with the external surface remaining for further adsorption. Indeed, the inflection point appears in the sample with 60% PVP representing also the Type H3 loop **(Figure 4e)**, which is observed for materials with aggregates of plate-like particles giving rise to slit-like pores.[42-44]

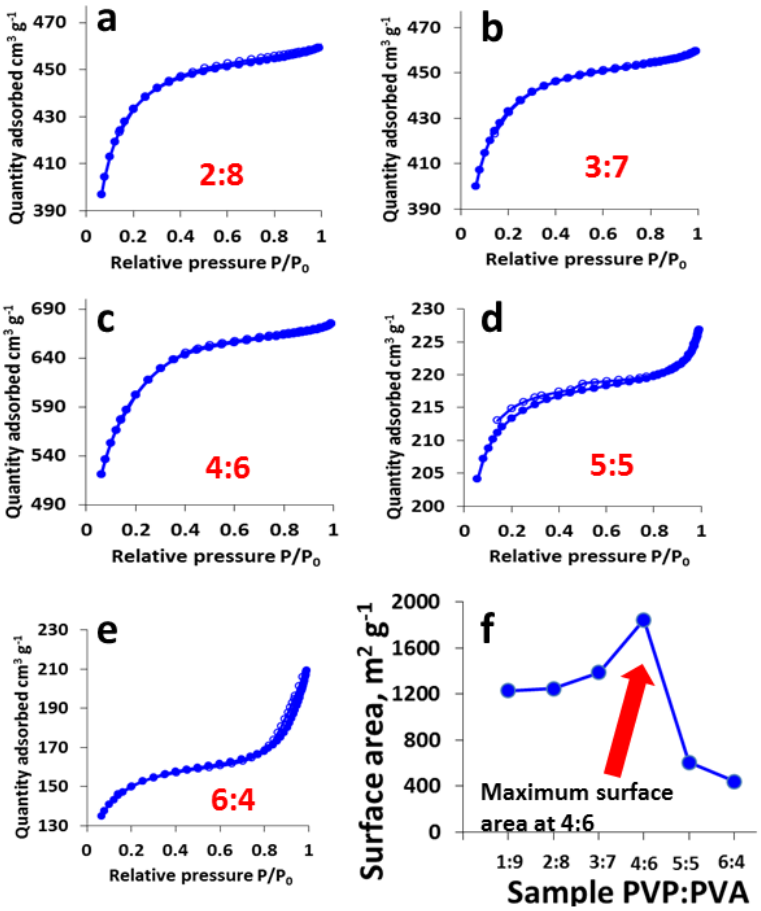

Figure 4. (a-e) gas adsorption/desorption isotherms of various samples with increasing mass ratio of PVP to PVA at carbonization/activation temperature of 700°C, (f) BET surface area of different sample with increasing ratio of PVP and a maximum at the PVP to PVA ratio of 4:6 (reaching to a surface area of 1846 m^2 g^{-1}). Filled and hollow circles in isotherms represent respectively the adsorption and desorption of nitrogen at -196°C and relative pressure P/P_0 0.0 to 1.0.

Combining now the observation from SEM data and N_2 gas adsorption/desorption isotherms, the following assumptions, have been made. The broken platelet shape is present without a continuous external surface structure. The end of one of the sheets the carbon sample with a PVP to PVA ratio of 4:6 shows a "cheddar-cheese''- like structure with a corresponding width of about 3 µm. This is indicative of the presence of a high number of small pores with respect to the other carbon samples investigated. Although the surface observation of the different carbon samples shows the presence of pores, yet there is an increasing degree of pore coverage with an increase in the

proportion of PVP introduced to preliminary composition. This means that the carbon material obtained from PVP: PVA ratio 4:6 based hydrogel exhibits the highest pore coverage. An exception is also found in the last samples with PVP: PVA ratio 5: 5 and 6: 4 which did not exhibit definite pore structures. Keeping in view the N_2 sorption curve, one can infer that the slit-like pores are expected to be found for such structures.

For all the prepared carbons, uneven size of pore diameter for ratio 1:9 to 4:6 are clearly visible. Large nano-meter sized pores in the range of 400 nm to 600 nm are mostly exhibited by the 1:9 sample; these sizes decrease with the 2:8 sample which showed mostly 200-300 nm diameter pore sizes. The carbons obtained after activation of 3:7 and 4:6 samples both possess large pore diameters looking like ‘’pores-within-pores’’ structures. The carbon material from 4:6 samples still retains some of the singular 100 nm diameter big pores and an average pore diameter of 2.36 nm (**Table S1** in *supporting information*). The specific surface area values increase steadily for the carbon samples with PVP to PVA ratio 1:9 to 4:6 with a sharp decline at ratio 5:5 as also seen from the BET values **(Figure 4f and Table 2)**. The SEM images show the availability and the morphology of the pores (Figure S5 in *supporting information*), which follows a similar pattern as the values of obtained specific surface area. The carbon samples with the high number of pores and with more complicated structures give an insight into the rate at which gases evolve from the surface of the carbon sample during activation of the corresponding ‘parent hydrogel’. This clearly shows the richness of the porosity and subsequent surface area of obtained carbon materials. Hence, by systematically varying the precursor composition, we can confirm that majority of bulk precursor material has been utilized for the pore development.

Table 2. Increasing mass ratio of PVP to PVA (for preparing the precursor hydrogel material) versus the BET surface area of derived carbons.

Sample	1:9	2:8	3:7	4:6	5:5	6:4
BET (m^2 g^{-1})	1230	1249	1347	1846	606	440

Influence of graphene as an additive on textural properties of carbon

At the next stage, lab-scale produced graphene was introduced to the polymer-based hydrogel to enhance the conductivity and elaborate the pore structure. For this purpose, graphene was used as an additive to the initial mixture of PVP to PVA mass ratio of 4:6 before the microwave treatment. As shown in Figure 2, the interaction with graphene gives structural stability and improves the pore architecture and thereby retaining the integrity of electrode materials via enhanced pore connectivity and easy access to the transport channels within the carbon matrix. A gradual increase of graphene mass ratio to the total mixture of PVP: PVA did not alter the morphology of the hydrogel obtained after microwave treatment. Therefore, one can expect the evolution of a similar pore structure in the hydrogel before it goes through KOH activation. As seen in **Table 3**, a gradual increase of graphene from 0.0081 wt./wt.% (0.010 wt./vol%) to 0.024 wt./wt.% (0.030 wt./vol%) results in enhanced surface area of the carbon material obtained after carbonization and activation at 700°C. **Figure 5** shows the simultaneous gas adsorption isotherm and thermogravimetry (TG) data of each sample obtained after activation of three-component mixture of PVP: PVA (4:6) with graphene at varying mass proportion. The sample without the addition of graphene exhibits a surface area of 1846 m^2 g^{-1}. The use of graphene improves the surface area of the resulting composite material up to ca. 3100 m^2 g^{-1}. The additional benefit of using graphene with polymer structure is to incorporate it within the layer structure (evident from low mass loss of ~4% in TGA curves), and the presence of such architecture preserves the integrity of carbon materials and keeps the channels open for ionic transport.

Table 3. Table 2. Porous textural data of activated carbons obtained from different proportion of wt. % of graphene in the mixture of PVP to PVA (4:6) at activation temperature T_C = 700ºC. For comparison, porous data of sample without graphene additive is given.

Sample	wt./wt.% of graphene	wt./vol.% of graphene	BET [$m^2\ g^{-1}$]	[a]V_{micro} [$cm^3\ g^{-1}$]	[b]V_{total} [$cm^3\ g^{-1}$]	[c]Pore diameter [nm]
C46P	-	-	1846	0.50	1.04	2.36
C46P-G10	0.008	0.01	2848	0.51	0.84	2.40
C46P-G20	0.016	0.02	3107	0.56	0.88	2.35
C46P-G30	0.024	0.03	2998	0.52	0.70	2.21

[a)] t-Plot micropore volume; [b)] BJH Desorption cumulative volume of pores between 1.7 nm and 300 nm diameter; [c)] BJH Desorption average pore diameter (4V/A).

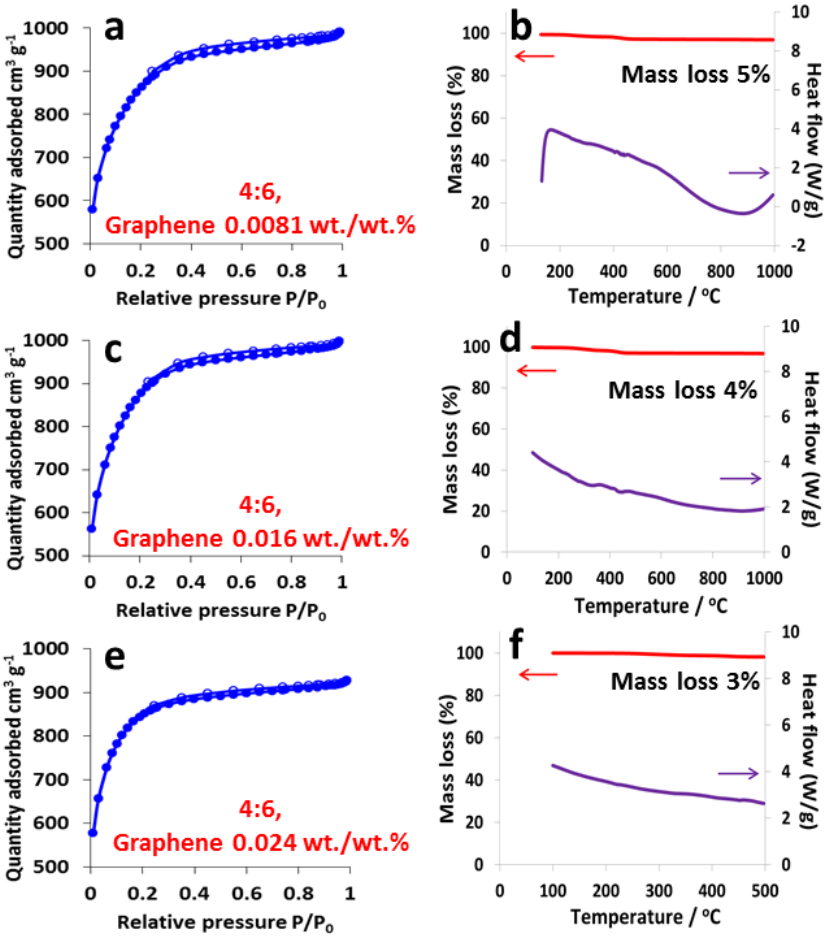

Figure 5. Isotherms for nanoporous carbon samples obtained from PVP:PVA (4:6) composite with increasing proportion of graphene (a-b) 0.0081 wt./wt.%, samples named in Table 3 as C46P-G10 (c-d) 0.016 wt./wt.%, sample named as C46P-G20 and (e-f) 0.024 wt./wt.% , sample named as C46P-G30 – carbonized and activated at 700°C and various analyses performed on the materials such as (a, c, e) gas adsorption characterization, and (d, d, f) thermogravimetric analysis.

One can see that the combination of PVP: PVA with graphene not only improves the surface area and alters the pore structure but also enhances pore connectivity and gives control over the pore alignment (Figure S6). This aspect is crucial for designing efficient charge storage systems where the compatibility of ion sizes with the size of pores is important.[45-47] As expected, the addition of graphene to the hydrogels increases their surface area and conductivity. With an increased amount of 0.016 wt./wt.% of graphene, the surface area up to 3107 m^2 g^{-1} is achieved (Table 3). However, a further increase of graphene content does not influence to greater extent the specific surface area and the pore architecture which is indicated by the sample containing 0.024 wt./wt.% graphene. The presence of micropore volume in the range of 0.5 cm^3 g^{-1} is similar to most commercial carbons, however, the presence of graphene sheets and their layer-by-layer connectivity with preserved stacking properties gives access to even small micropores which enhance the surface area.[48-49] Moreover, a well-distributed pore size range makes these carbons suitable for preparing sustainable electrodes for supercapacitors which have been investigated and discussed in the next section.

Performance of nanoporous carbons in symmetric supercapacitors

Electrochemical performance of symmetric supercapacitors using two types of carbon samples i) PVP to PVA mass ratio of 4:6 (referred to in this section as PVP+PVA) and ii) PVP to PVA mass ratio of 4:6 with 0.016 wt./wt.% of graphene (referred in this section as PVP+PVA+Graphene) is compared and summarized in **Figure 6**. Keeping in view the wide pore size distribution and pore diameter in the range of 2.36 nm, the alkali metal ions and most of the inorganic cations would easily fit resulting in fast charging of EDL. We selected $NaNO_3$ based electrolyte due to its easy availability, low cost, abundance, and, most of all, the compatibility of ions size with pore structure of designed carbons. The symmetric charge/discharge curves for a capacitor with PVP+PVA based

carbon at 0.2 A g^{-1} (Figure S9-S11 in *supporting information*) and nearly rectangular shape of CVs at high scan rate up to 200 mV s^{-1} from 0.8 V up to 1.6 V suggests the main charge storage phenomenon occurring at the electric double layer (EDL). Similarly, the second capacitor using PVP+PVA+graphene based electrode also shows symmetric charge/discharge curves and excellent charge propagation up to 1.6 V and 200 mV s^{-1}. Nevertheless, due to the presence of water based electrolyte, some contributions indicated by the current increase in CVs at the high voltage region near 1.5 or 1.6 V are important which correspond to the reversible adsorption/desorption (or reversible storage) of hydrogen in pores of the negative electrode material produced under the electrochemical reduction of water.[50] Furthermore, High voltages up to 1.6 V are possible with such supercapacitor using neutral aqueous $NaNO_3$ electrolyte owing to high overpotential at the negative carbon electrode associated with the increase of local pH. However, these faradaic processes represent only a fractional contribution to the total capacitance of the supercapacitor. Certainly, the main capacitance in both the systems originates from charge storage at the EDL. The comparison of CVs (Figure S10c) and galvanostatic charge/discharge (Figure S10d) between the two capacitors confirm the high capacitance for the system with an electrode containing the graphene as an additive. One can also see that, despite the low capacitance for the cell using PVP+PVA based electrode, the shape of the CV and GCPL curves is more symmetric suggesting EDL charging as the main charge storage phenomenon. In particular, the rectangular shape of CV and symmetric GCPL for PVP+PVA based sample up to 200 mV s^{-1} and 5 A g^{-1} (Figure S9) indicates the total charge storage at the EDL which is a highly reversible and physical phenomenon and involves very little contribution from the electrochemical reduction/oxidation of water at the negative or positive carbon electrodes. Thanks to the polymeric structure preserving the electrode porous structure, a highly fast charge and discharge can be

achieved, and thereby an enhanced rate performance of the supercapacitor device. A low ohmic loss in charge/discharge curves is evident of good pore connectivity and transport channels within the electrode matrix for ionic movement. As the triangular shape of charge/discharge curves is conserved even at high specific currents, one can infer the high rate capability and cycle life of supercapacitor using this electrode material.

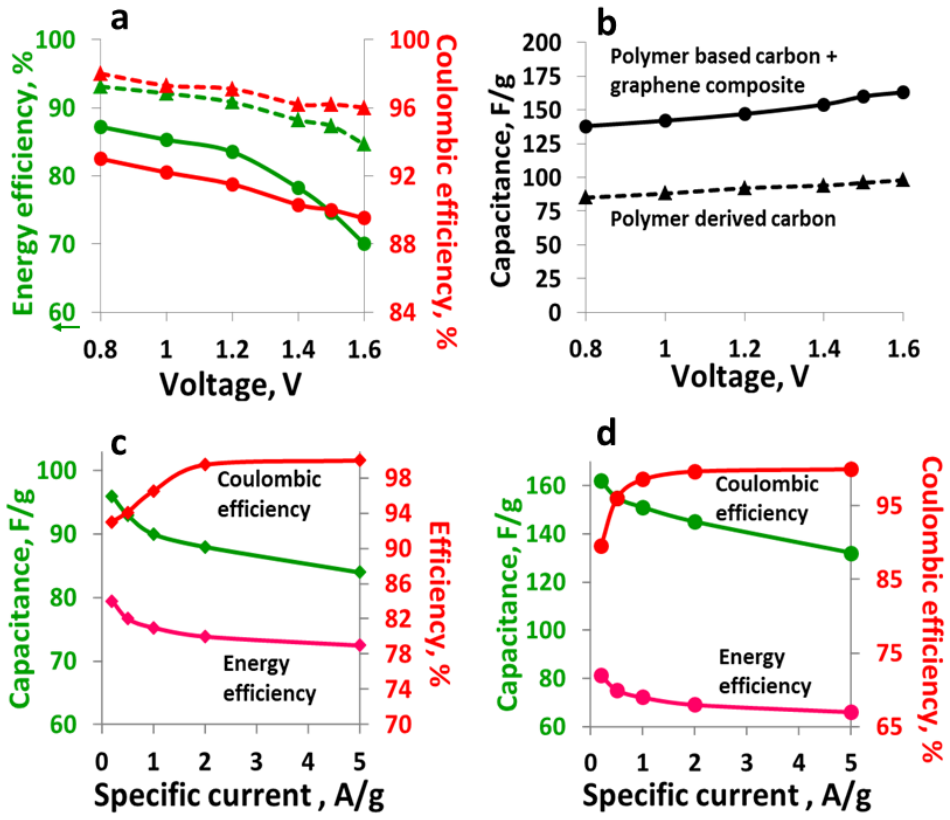

Figure 6. Electrochemical performance of symmetric capacitor using PVP+PVA and PVP+PVA+graphene electrodes in 5 mol L^{-1} $NaNO_3$; (a-b) evolution of coulombic efficiency (η_c), energy efficiency (η_e) and capacitance versus voltage up to 1.6 V at 0.2 A g^{-1}, and capacitance, coulombic efficiency, energy efficiency evolution at 1.6 V with increasing specific current up to 5 A g^{-1} for (c) PVP+PVA based capacitance and (d) PVP+PVA+graphene based supercapacitor. The dashed and solid lines represent the PVP+PVA and PVP+PVA+graphene based supercapacitors respectively.

Figure 6a-d shows the comparison of coulombic efficiency (ratio of the discharge time to charging time), energy efficiency (ratio of area under discharge curve to the area under charging curve),

capacitance, and, rate performance. Relatively, high value of energy efficiency (89%) and coulombic efficiency (96%) at 1.6 V (at 0.2 A g^{-1} in Figure 6a) for the cell with PVP+PVA based electrodes suggest the easy ionic transport within the channels and without the substantial loss of charges in the faradaic processes. This is also evidence of fast charging/discharging of EDL in the case of PVP+PVA based capacitor. On the other hand, for the supercapacitors with PVP+PVA+graphene based electrodes, the energy efficiency value is 73% and the coulombic efficiency value is 89% at 1.6 V (at 0.2 A g^{-1}). The relatively low efficiency values suggest the presence of deep channels between the graphene layers with slight coverage due to the functional groups which may hinder the swift movement of ions upon charge and discharge.

The capacitance comparison in Figure 6b and the evolution of capacitance versus increasing specific current (Figure 6c-d) suggest a high rate performance of supercapacitor constructed by using PVP+PVA electrode material. Although the capacitance value for the supercapacitor with PVP+PVA+graphene electrode are high (163 F g^{-1} at 0.2 A g^{-1}), yet the decrease in capacitance at high specific current is 18% from 0.2 A g^{-1} to 5 A g^{-1}. This is also indicated by the low energy efficiency of supercapacitor using this material ~66% at 5 A g^{-1} compared to ~79% for PVP+PVA based cell. Indeed the low energy efficiency for the cell using electrode material with graphene additive suggests a different pore architecture and the presence of functional groups.

The Nyquist plot, which is the frequency responses of the device with imaginary and real impedances as a function of the frequency is shown in **Figure 7**. The high-frequency intersection with the positive Z-axis shows a semicircle at this frequency domain, a 45° line region, and a vertical line in the low-frequency region typically signifies the charge storage mechanisms of the capacitive materials. The presence of functional groups on the surface of the carbon materials may contribute to the charge transfer process that arises from an electron transfer from one phase (e.g.

electrode) to another (e.g. liquid). In addition, interfacial impedances between the current collector/active material may also contribute to the appearance of the semicircle.[51-53] This was confirmed by recording the impedance data at multiple potentials from the open circuit potential to 1.6 V. The change in the charge transfer resistance (diameter of the semicircle) with increasing potential affirm the assertion that main contribution is from a charge transfer process. The R_{ct} values range from 0.33 to 0.61 Ω for Figure 7a (PVP+PVA) and 0.14 to 0.23 Ω for 7b (PVP+PVA+graphene), as the voltage increases. Furthermore, the smaller values for the Rct obtained at high frequencies for the cell with PVP+PVA+graphene based electrodes as the voltage increases is attributed to increase in conductivity of the carbon material due to the presence of graphene, and may increase electron mobility as the voltage increases leading to decrease in the diameter of the semicircle. ESR values in **Table 4** extracted from the Nyquist plot at 1 kHz show an increasing trend for both the capacitors from OCV to 1.6 V. Nevertheless, these values are smaller in PVP+PVA+Graphene electrodes based capacitor than in PVP+PVA based capacitor, owing to high interlayer connectivity in the latter. Additionally, the ESR values measured from the galvanostatic charge/discharge curves at 1 A g^{-1} (up to 1.6 V) also follow a similar pattern, with 0.381 Ω for PVP+PVA based capacitor and 0.261 Ω for the capacitor with PVP+PVA+graphene electrodes.

Table 4. ESR and time constant (τ) values for symmetric supercapacitors with PVP+PVA and PVP+PVA+Graphene based carbon electrodes in 5 mol L^{-1} $NaNO_3$.

		OCV	0.8 V	1.0 V	1.2 V	1.4 V	1.5 V	1.6 V
PVP+PVA	ESR (Ω)	0.543	0.580	0.620	0.631	0.664	0.798	0.982
	τ (s)	1.41	1.41	1.41	1.41	1.89	1.89	1.89
PVP+PVA +Graphene	ESR (Ω)	0.438	0.438	0.451	0.460	0.472	0.524	0.575
	τ (s)	2.27	1.89	1.89	1.89	1.89	1.89	1.89

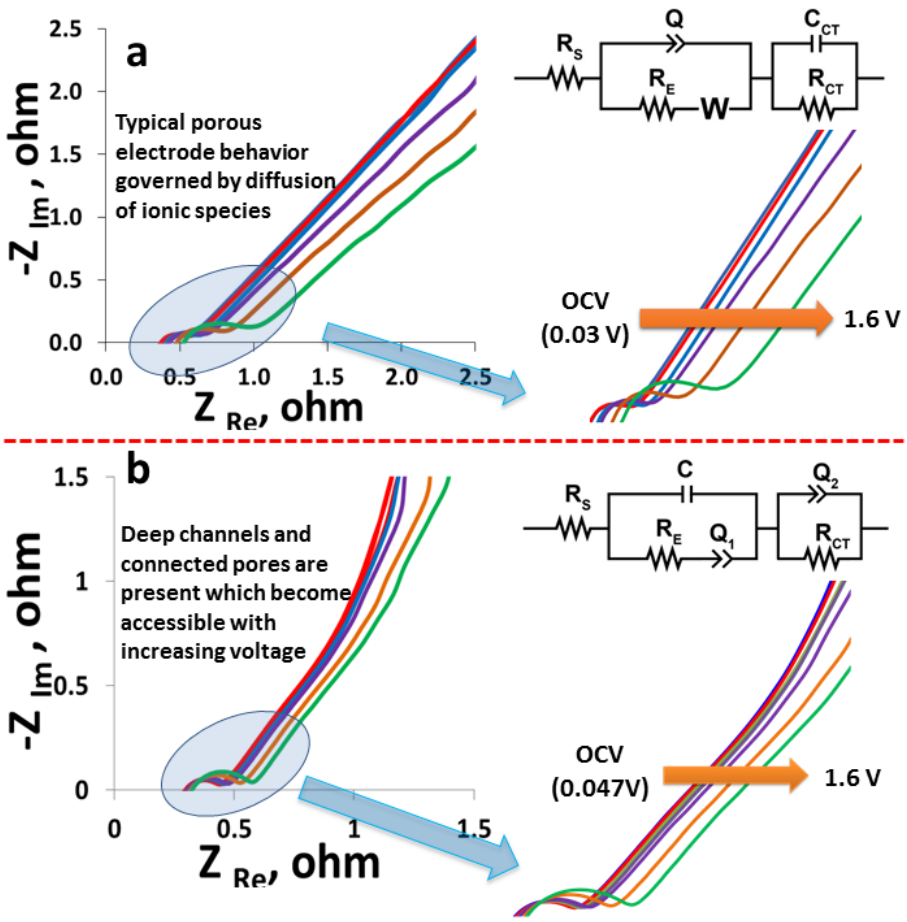

Figure 7. (a) Nyquist plots obtained at different voltage from open circuit voltage up to 1.6 V for symmetric capacitors using (a) PVP+PVA based electrodes and (b) PVA+PVP+graphene electrodes in 5 mol L^{-1} $NaNO_3$. The insets in 'a' and 'b' show the equivalent circuit models for the symmetric cells, and the color representation for voltages is as follows: Red (OCV), light blue (0.8 V), yellow (1.0 V), blue (1.2 V), purple (1.4 V), orange (1.5 V) and green (1.6 V).

Furthermore, the shift of the knee frequency region suggests the influence of increasing voltage on the ionic movement. The impeded movement of ions within the deeper pores is indicated by extended medium frequency region. Equivalent circuit diagram obtained from the fitting of impedance data are presented for both systems in Figure 7. In the equivalent circuit, the equivalent circuit used for fitting of the EIS plots in this work is shown in Figure 7 a and b. The EIS plots are fitted according to the Randle's model, which is ideal and close to practical application. The

equivalent circuit element such as the R_S and R_{CT} are shown in Table S3. Rs is the equivalent series resistance (ESR), which depicts the resistance of the electrolyte combined with the internal resistance of the electrode, R_{CT} is the resistance of the electrode-electrolyte interface. CPE_{DL} is the constant phase element (CPE) of double layer, symbolizes the double layer capacitance, which occurs at interfaces between the porous carbon and solution due to separation of ionic and/or electronic charges. The mathematical definition for CPE is expressed as [H. Li, J. Wang, Q. Chu, Z. Wang, F. Zhang, S. Wang, Theoretical and experimental specific capacitance of polyaniline in sulfuric acid, J. Power Sources 190 (2009) 578–586.]:

$$CPE = \frac{1}{Q_0(j\omega)^n} \tag{8}$$

Where Q_0 and n are frequency-independent constants and ω is the angular frequency. The exponent n is a correction factor which is related to the capacitive kinetics and roughness of electrode surfaces. The values for n range between 0 and 1; n = 1 denotes that the CPE is an ideal capacitor, for n = -1, CPE behaves as an inductor, while. n = 0 and 0.5 denote a resistance and Warburg behavior respectively.

W is the Warburg element, which represents the diffusion of ions into the porous electrode in the mid frequency region, and is a consequence of the frequency requirement of the diffusion process. A probable attribute to the insensitivity to changing voltage is a short diffusion path length of the ions in the electrolyte, as evidenced by a short Warburg region on the Nyquist plots. R_L represent the leakage and faradaic resistance, which is placed in parallel with CPE_L, and it is usually very high and can be ignored in the circuit however we reported in our model. CPE_L represents pseudocapacitance, which arises with voltage dependent Faradaic charge transfer processes. The n in equation 8 for the CPE_L in Figure 7a is ~0.7 while the n value in Figure 7b ~ 1. The time

constant calculated from the real capacitance versus frequency data [54] (Figure S12-13) for the two systems is presented in Table 4. Both the supercapacitors can be fully charged up to 1.6 V in a similar time of 1.89 s which confirms the positive effect of graphene additive on the carbon nanostructure (despite high surface area) for improved the rate performance.

Galvanostatic charge/discharge cycling test of supercapacitor containing PVP+PVA and PVP+PVA+graphene based electrodes in 5 mol L^{-1} $NaNO_3$ electrolyte at 1.6 V and a constant specific current of 1 A g^{-1} were performed **(Figure 8)**. At the end of 10,000 galvanostatic charge/discharge cycles, capacitance remains constant (no capacitance decay) for the capacitor with PVP+PVA electrodes while it decays by 4% for the cell with PVP+PVA+graphene based electrodes. However, the energy efficiency estimated after every 1000 galvanostatic charge/discharge cycle improves by 2 and 4% after total of 10,000 cycles for PVP+PVA and PVP+PVA+graphene based systems respectively. The improved energy efficiency could be due to the enhanced wetting of electrode and gradual ions transport into the deep pores of the electrodes. In particular, for the PVP+PVA based capacitor, the constant capacitance and efficiency values suggest the stability of the supercapacitor device to operate at high voltage and with negligible degradation to the electrodes. A comparison of galvanostatic charge discharge curves at 1 A g^{-1} before and after cycling shows superimposition of curves corroborating the high stability of the system, where both cells maintain nearly the initial 'fresh cell-like' characteristics. The energy and power performance estimated from galvanostatic charge/discharge up to high specific currents is shown in Ragone plot (Figure 8d), where PVA+PVP and PVA+PVP+graphene based capacitors demonstrate high energy of 8 and 12 Wh kg^{-1} respectively at a specific power of 2 kW kg^{-1} (Table S2). Furthermore, the surface area of carbons obtained from activation of polymeric sources and the performance of thereafter-built supercapacitors in aqueous electrolytes

is compared in **Table 5.** High surface area and capacitance values obtained for carbons prepared in this work closely match and in some cases exceed the performance of state-of-the-art systems.

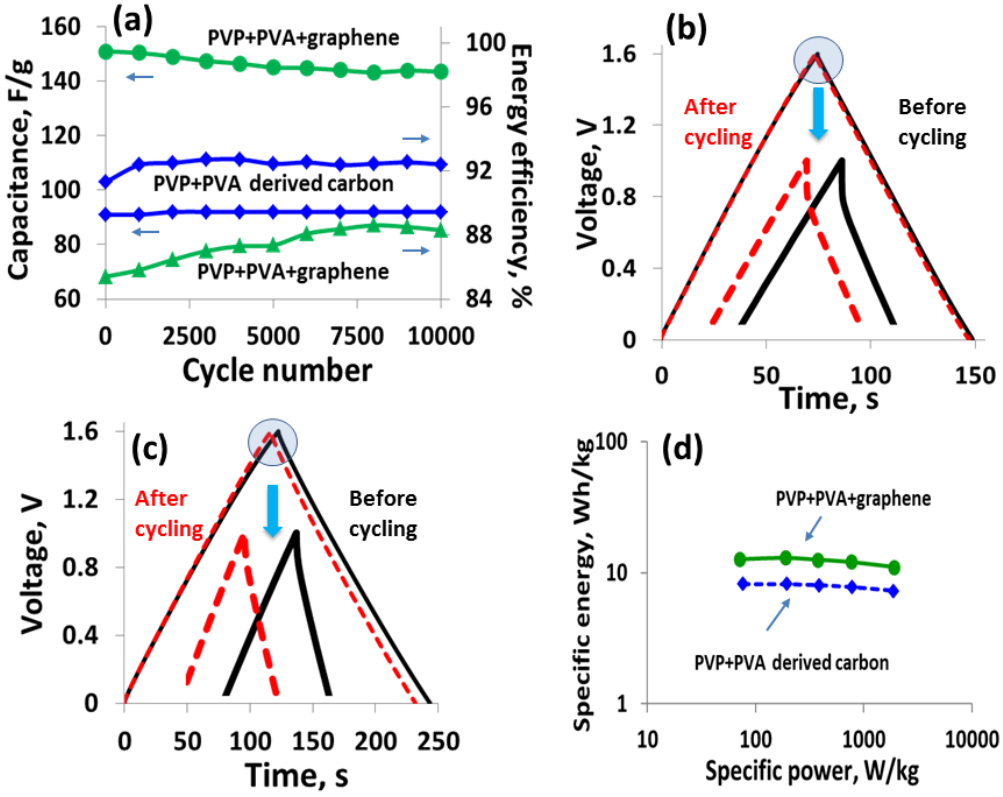

Figure 8. (a) Electrochemical stability test of supercapacitors for 10000 galvanostatic charge/discharge cycles at 1.0 A/g, comparison of galvanostatic charge/discharge curves before and after cycling at 1 A/g for (b) PVP+PVA carbon based supercapacitor and (c) PVP+PVA+graphene composite based supercapacitor. (d) Ragone plot presenting the comparison of energy and power performance for symmetric supercapacitors with two carbon materials. The data for Ragone plot is extracted from the galvanostatic charge/discharge curves at 0.2 A g^{-1}, 0.5 A g^{-1}, 1 A g^{-1}, 2 A g^{-1} and 5 A g^{-1} up to 1.6 V in Figure S9.

Table 5. Comparison of surface area, capacitance and density of supercapacitors using polymers derived carbons in aqueous electrolytes.

Materials	Specific surface area ($m^2 g^{-1}$)	Specific capacitance ($F g^{-1}$)	Energy density ($Wh kg^{-1}$)	Ref.
Low-density polyethylene (LDPE)-derived activated carbons (PE-AC)	1600	112	-	55
Phenolic resin	1759	115	-	56
Graphene foam/polyvinyl alcohol/formaldehyde (GF/PVA/FP and GF/PVA/F)	705 610	158 177	- -	57
Nitrogen-doped hollow carbon spheres	-	173	-	58
Lignin-based hierarchical porous carbon	1140	148 at 0.2 A g^{-1}	-	59
Sodium lignosulfonate	1867	370 at 0.5 A g^{-1}	18.5	60
Block copolymer	2104	257 at 0.5 A g^{-1}	-	61
Block copolymers	953	150 at 0.625 A g^{-1}	-	62
Polyacrylonitrile	451	156 at 0.2 A g^{-1}	-	63
Eucalyptus-bark	1276	155	32.8	64
Lecithin	1803	285 at 0.5 A g^{-1}	24.7	65
PVP+PVA+graphene	3107	163 at 0.2 A g^{-1}	12	This work

CONCLUSIONS

Nanoporous carbons derived from the composite of PVP and PVA represent an eco-friendly and low cost route to prepare electrode materials. The systematic variation of polymeric components gives control over the evolution of porous texture which can be adapted for charge storage applications. Interestingly, the chemical reaction via microwave irradiation resulting in hydrogel gives control over porosity at the precursor level. By introducing graphene additives to the

preliminary composite before activation, certain physicochemical and electrochemical properties of the carbon material can be altered. The addition of graphene improves the surface area and pore connectivity which in turn provides facile transport channels for ionic movement. The charge/discharge curves of symmetric supercapacitors confirm that by adapting the majority of pores to the size of ions, the performance of supercapacitor device can be improved. The outstanding energy and power parameters of supercapacitors show great potential for the application of these materials in high-power related applications. Hence, designing materials with pores adaptable to ions size is crucial for next-generation high power devices. Future work is aimed at designing new carbons based on these reaction pathways and activation processes by the use of different polymeric chain lengths to create new pore architectures that could accommodate bigger ions e.g., ionic liquid-based electrolytes.

ASSOCIATED CONTENT

Supporting Information Available: This material is available free of charge via the Internet at http://pubs.acs.org

Steps during preparation of carbons; gas adsorption data of carbons; SEM images of carbons; porous textural data of carbons; Raman and XRD spectra of selected carbon samples; Electrochemical performance comparison of supercapacitors;

AUTHOR INFORMATION

Corresponding authors

Farshad Barzegar

Electrical, Electronic and Computer Engineering Department, University of Pretoria,

Pretoria 0002, South Africa

Email: farshad.barzegar@up.ac.za

Qamar Abbas

Institute for Chemistry and Technology of Materials, Graz University of Technology,

Stremayrgasse 9, 8010 Graz, Austria

Email: qamar.abbas@tugraz.at

Authors

Vladimir Pavlenko - Al-Farabi Kazakh National University, 71 al-Farabi Ave., 050040 Almaty, Kazakhstan

Muhammad Zahid - Department of Chemistry, University of Agriculture, 38000 Faisalabad, Pakistan

Abdulhakeem Bello - Department of Theoretical and Applied Physics, African University of Science and Technology, Km. 10 Airport Road, Galadimawa, Abuja, Nigeria

Department of Physics, University of Pretoria, Pretoria 0002, South Africa

Xiaohua Xia - Electrical, Electronic and Computer Engineering Department, University of Pretoria, Pretoria 0002, South Africa

Ncholu Manyala - Department of Physics, University of Pretoria, Pretoria 0002, South Africa

Kenneth I. Ozoemena - School of Chemistry, Molecular Science Institute, University of the Witwatersrand, Private Bag 3, P O Wits, Johannesburg 2050, South Africa

Author contributions

Q.A and F.B conceptualized the work. F.B prepared and characterized carbon materials. F.B, V.P and M.Z performed physicochemical data analysis. F.B conducted electrochemical investigations and data analysis supported by Q.A. F.B, V.P and M.Z wrote the first draft and A.B, X.X, N.M, K.O and Q.A reviewed the final manuscript.

Notes

The authors declare no competing financial interest.

ACKNOWLEDGEMENTS

This work is supported by the National Research Foundation of South Africa (Grant Numbers: 61056). The findings and recommendations expressed in this work are that of the authors and the NRF does not accept any liability in this regard. Q.A acknowledges the Austrian Science Fund (FWF) for granting Lise Meitner project M2576-N37, and support from Bernhard Gollas, Ilie Hanzu and Martin Wilkening.

REFERENCES

1. Pomerantseva, E.; Bonaccorso, F.; Feng, X.; Cui, Y.; Gogotsi, Y. Energy storage: The future enabled by nanomaterials. *Science* **2019**, *366*, eaan8285.

2. Borenstein, A.; Hanna, O.; Attias, R.; Luski, S.; Brousse, T.; Aurbach, D. Carbon-based composite materials for supercapacitor electrodes: a review. *J. Mater. Chem. A* **2017**, *5*, 12653-12672.

3. Gonzalez, A.; Goikolea, E.; Barrena, J.; Mysyk, R. Review on supercapacitors: Technologies and materials. *Renewable and Sustainable Energy Reviews* **2016**, *58*, 1189-1206.

4. Gao, Y. Graphene and Polymer Composites for Supercapacitor Applications: a Review. *Nano Review*, **2017**, *12*, 387.

5. Borchardt, L.; Oschatz, M.; Kaskal, S. Tailoring porosity in carbon materials for supercapacitor applications. *Mater. Horiz.*, **2014**, *1*, 157-168.

6. Pipitone, E.; Vitale, G. A regenerative braking system for internal combustion engine vehicles using supercapacitors as energy storage elements - Part 1: System analysis and modeling. *J. Power Sources* **2020**, *448*, 227368.

7. Zou, Z.; Cao, J.; Cao, B.; Chen, W. Evaluation strategy of regenerative braking energy for supercapacitor vehicle. *ISA Transaction*, **2015**, *55*, 234-240.

8. Monteiro Baptista, J.; Sagu, J.; Wijayantha, KG.; Lobato, K. State-of-the-art materials for high power and high energy supercapacitors: Performance metrics and obstacles for the transition from lab to industrial scale – A critical approach. *Chemical Engineering Journal*, **2019**, *374*, 1153-1179.

9. Gratuito, M.; Panyathanmaporn, T.; Chumnanklang, R.; Sirinuntawittaya, N.; Dutta, A. Production of activated carbon from coconut shell: Optimization using response surface methodology. *Bioresource Technology*, **2008**, *99*, 4887-4895.

10. Foo, K.; Hameed, B. Preparation and characterization of activated carbon from pistachio nut shells via microwave-induced chemical activation. *Biomass and Bioenergy*, **2011**, *35*, 3257-3261.

11. Kleszyk, P.; Ratajczak, P.; Skowron, P.; Jagiello, J.; Abbas, Q.; Frackowiak, E.; Béguin, F. Carbons with narrow pore size distribution prepared by simultaneous carbonization and self-activation of tobacco stems and their application to supercapacitors. *Carbon*, **2015**, *81*, 148-157.

12. Salitra, G.; Soffer, A.; Eliad, L.; Cohen, Y.; Aurbach, D.; Carbon Electrodes for Double-Layer Capacitors I. Relations Between Ion and Pore Dimensions. *J. Electrochem. Soc.*, **2000**, *147*, 2486-2493.

13. Eliad, L.; Pollak, E.; Levy, N.; Salitra, G.; Soffer, A.; Aurbach, D. Assessing optimal pore-to-ion size relations in the design of porous poly(vinylidene chloride) carbons for EDL capacitors. *Appl. Phys. A*, **2006**, *82*, 607-613.

14. Eliad, L.; Salitra, G.; Soffer, A.; Aurbach, D. Ion Sieving Effects in the Electrical Double Layer of Porous Carbon Electrodes: Estimating Effective Ion Size in Electrolytic Solutions. *J. Phys. Chem. B*, **2001**, *105*, 6880-6887.

15. Li, Z.; Gadipelli, S.; Li, H.; Howard, C.; Brett, D.; Shearing, P.; Guo, Z.; Parkin, I.; Li, F. Tuning the interlayer spacing of graphene laminate films for efficient pore utilization towards compact capacitive energy storage. *Nature Energy* **2020**, *5*, 160-168.

16. Ania, C.; Pernak, J.; Stefaniak, F.; Raymundo-Piñero, E.; Béguin, F. Solvent-free ionic liquids as in situ probes for assessing the effect of ion size on the performance of electrical double layer capacitors. *Carbon*, **2006**, *44*, 3126-3130.

17. Ortega, P.; A dos Santos Jr., G.; Trigueiro, P.; Silva, G.; Quintanal, N.; Blanco, C.; Lavall, R.; Santamaria, R. Insights on the Behavior of Imidazolium Ionic Liquids as Electrolytes in Carbon-Based Supercapacitors: An Applied Electrochemical Approach. *J. Phys. Chem. C*, **2020**, *124*, 15818-15830.

18. Largeot, C.; Portet, C.; Chmiola, J.; Taberna, P.L.; Gogotsi, Y.; Simon, P. Relation between the Ion Size and Pore Size for an Electric Double-Layer Capacitor. *J. Am. Chem. Soc.*, **2008**, *130*, 2730-2731.

19. Matsuoka, K.; Yamagishi, Y.; Yamazaki, T.; Setoyama, N.; Tomita, A.; Kyotani, T. Extremely high microporosity and sharp pore size distribution of a large surface area carbon prepared in the nanochannels of zeolite Y. *Carbon*, **2005**, *43*, 876-879.

20. Hulicova, D.; Yamashita, J.; Soneda, Y.; Hatori, H.; Kodama, M. Supercapacitors Prepared from Melamine-Based Carbon. *Chem. Mater.*, **2005**, *17*, 1241-1247.

21. Hulicova, D.; Kodama, M.; Hatori, H. Electrochemical Performance of Nitrogen-Enriched Carbons in Aqueous and Non-Aqueous Supercapacitors. *Chem. Mater.*, **2006**, *18*, 2318-2326.

22. Inagaki, M.; Toyoda, M.; Soneda, Y.; Tsujimura, S.; Morishita, T. Templated mesoporous carbons: Synthesis and applications. *Carbon*, **2016**, *107*, 448-473.

23. Ding, L.; Gao, H.; Xie, F.; Li, W.; Bai, H.; Li, L. Porosity-Enhanced Polymers from Hyper-Cross-Linked Polymer Precursors. *Macromolecules*, **2017**, *50*, 956-962.

24. Hua Zhu, J.; Chen, Q.; Sui, Z-Y.; Pan, L.; Yu, J.; Han, B-H.; Preparation and adsorption performance of cross-linked porous polycarbazoles. *J. Mater. Chem. A*, **2014**, *2*, 16181-16189.

25. Seo, M.; Kim, S.; Oh, J.; Kim, S-J.; Hillmyer, M. Hierarchically Porous Polymers from Hyper-cross-linked Block Polymer Precursors. *J. Am. Chem. Soc.*, **2015**, *137*, 600-603.

26. Yenisoy-Karakas, S.; Aygun, A.; Gunes, M.; Tahtasakal, E.; Physical and chemical characteristics of polymer-based spherical activated carbon and its ability to adsorb organics. *Carbon*, **2004**, *42*, 477-484.

27. Gyu Park, H.; Won Kim, T.; Yun Chae, M.; Yoo, I-K. Activated carbon-containing alginate adsorbent for the simultaneous removal of heavy metals and toxic organics. *Process Biochemistry*, **2007**, *42*, 1371-1377.

28. Makromaski, G. Porous structure and thermal properties of carbon adsorbents from pitch–polymer compositions. *Journal of Thermal Analysis and Calorimetry*, **2018**, *133*, 1345-1352.

29. Raymundo-Pinero, E.; Leroux, F.; Béguin, F. A High-Performance Carbon for Supercapacitors Obtained by Carbonization of a Seaweed Biopolymer. *Adv. Mater.*, **2006**, *18*, 1877-1882.

30. Zhang, L.; Gu, H.; Sun, H.; Cao, F.; Chen, Y.; Chen, G. Molecular level one-step activation of agar to activated carbon for high performance supercapacitors. *Carbon*, **2018**, *132*, 573-579.

31. Kamoun, E.A.; Chen, X.; Mohy Eldin, M.S.; Kenawy, E.-R.S. Crosslinked poly(vinyl alcohol) hydrogels for wound dressing applications: A review of remarkably blended polymers. *Arab. J. Chem.*, **2015**, *8*, 1-14.

32. Swain, A.K.; Bahadur, D.; Enhanced Stability of Reduced Graphene Oxide Colloid Using Cross-Linking Polymers. *J. Phys. Chem. C.*, **2014**, *118*, 9450-9457.

33. Zhang, L.; Zhang, F.; Yang, X.; Long, G.; Wu, Y.; Zhang, T.; Leng, K.; Huang, Y.; Ma, Y.; Yu, A.; Chen, Y. Porous 3D graphene-based bulk materials with exceptional high surface area and excellent conductivity for supercapacitors. *Sci. Rep.*, **2013**, *3*, 1408.

34. Bello, A.; Fashedemi, O.O.; Lekitima, J.N.; Fabiane, M.; Dodoo-Arhin, D.; Ozoemena, K.I.; Gogotsi, Y.; Charlie Johnson, A.T.; Manyala, N.; High-performance symmetric electrochemical capacitor based on graphene foam and nanostructured manganese oxide. *AIP Adv.*, **2013**, *3*, 082118.

35. Guellati, O.; Janowska, I.; Bégin, D.; Guerioune, M.; Mekhalif, Z.; Delhalle, J.; Moldovan, S.; Ersen, O.; Pham-Huu, C.; Influence of ethanol in the presence of H_2 on the catalytic growth of vertically aligned carbon nanotubes. *Appl. Catal. A Gen.*, **2012**, *423–424*, 7-14.

36. Balducci, A.; Belanger, D.; Brousse, T.; Long, J. W.; Sugimoto, W. Perspective—A Guideline for Reporting Performance Metrics with Electrochemical Capacitors: From Electrode Materials to Full Devices. *J. Electrochem. Soc.*, **2017**, *164*, A1487-A1488.

37. Zhou, J.; Lian, J.; Hou, L.; Zhang, J.; Gou, H.; Xia, M.; Zhao, Y.; Strobel, T.; Tao, L.; Gao, G. Ultrahigh volumetric capacitance and cyclic stability of fluorine and nitrogen co-doped carbon microspheres. *Nature Communications*, **2015**, *6*:8503.

38. Derbyshire F., Jagtoyen, M., Thwaites, M., Activated Carbons-Production and Applications, in: J.W. Patrick, (Edit.).Porosity in Carbon, London, U.K.: Edward Arnold, **1995**; 227.

39. Marsh, H., Rodriguez-Reinoso, F. Activated Carbon. Elsevier Science & Technology Books, **2006;** 536.

H. Marsh, F. Rodriguez-Reinoso, Activated Carbon, London, U.K.: Elsevier, **2006**.

40. Shin, H.; Ryoo, R.; Kruk, M.; Jaroniec, M. Modification of SBA-15 pore connectivity by high-temperature. *Chemical Commun.*, **2001**, 349.

41. Lowe, J.; Baker, R. Deformation of Ordered Mesoporous Silica Structures on Exposure to High Temperatures. *J. Nanomater.*, **2014**, *2014*, 754076.

42. Wei, L.; Sevilla, M.; Fuertes, A.B.; Mokaya, R.; Yushin, G. Polypyrrole-Derived Activated Carbons for High-Performance Electrical Double-Layer Capacitors with Ionic Liquid Electrolyte. *Adv. Funct. Mater.*, **2012**, *22*, 827-834.

43. Sing, K. S. W.; Williams, R. T. Physisorption Hysteresis Loops and the Characterization of Nanoporous Materials. *Adsorpt. Sci. Technol.*, **2004**, *22*, 773-782.

44. Weidemann, S.; Kockert, M.; Wallacher, D.; Ramsteiner, M.; Mogilatenko, A.; Rademann, K.; Fischer, S. F. Controlled Pore Formation on Mesoporous Single Crystalline Silicon Nanowires: Threshold and Mechanisms. *J. Nanomater.*, **2015**, *2015*, 672305.

45. Prehal, C.; Koczwara, C.; Amenitsch, H.; Presser, V.; Paris, O. Salt concentration and charging velocity determine ion charge storage mechanism in nanoporous supercapacitors. *Nature Communications* **2018**, *9*:4145.

46. Prehal, C.; Koczwara, C.; Jäckel, N.; Schreiber, A.; Burian, M.; Amenitsch, H.; Hartmann, M.; Presser, V.; Paris, O. Quantification of ion confinement and desolvation in nanoporous carbon supercapacitors with modelling and in situ X-ray scattering. *Nature Energy* **2017**, *2*:16215.

47. Jäckel, N.; Simon, P.; Gogotsi, Y.; Presser, V. Increase in Capacitance by Subnanometer Pores in Carbon. *ACS Energy Lett.*, **2016**, *1*, 1262-1265.

48. Zheng, C.; Zhou, X.; Cao, H.; Wang, G.; Liu, Z. Synthesis of porous graphene/activated carbon composite with high packing density and large specific surface area for supercapacitor electrode material. *J. Power Sources* **2014**, *258*, 290-296.

49. Li, H.; Pan, L.; Nie, C.; Liu, Y.; Sun, Z. Reduced graphene oxide and activated carbon composites for capacitive deionization. *J. Mater. Chem.*, **2012**, *22*, 15556-15561.

50. Abbas, Q.; Ratajczak, P.; Babuchowska, P.; Comte, A. L.; Bélanger, D.; Brousse, T.; Béguin, F. Strategies to Improve the Performance of Carbon/Carbon Capacitors in Salt Aqueous Electrolytes. *J. Electrochem. Soc.*, **2015**, *162*, A5148-A5157.

51. Zhang, S.; Pan, N. Supercapacitors Performance Evaluation. *Adv. Energy Mater.*, **2015**, *5*, 1401401.

52. Mathis, T.; Kurra, N.; Wang, X.; Pinto, D.; Simon, P.; Gogotsi, Y. Energy Storage Data Reporting in Perspective—Guidelines for Interpreting the Performance of Electrochemical Energy Storage Systems. *Adv. Energy Mater.*, **2019**, *9*, 1902007.

53. Dsoke, S.; Tian, X.; Täubert, C.; Schlüter, S.; Wohlfahrt-Mehrens, M. Strategies to reduce the resistance sources on Electrochemical Double Layer Capacitor electrodes. *J. Power Sources* **2013**, *238*, 422-429.

54. Taberna, P. L.; Simon, P.; Fauvarque, J. F. Electrochemical Characteristics and Impedance Spectroscopy Studies of Carbon-Carbon Supercapacitors. *J. Electrochem. Soc.*, **2003**, *150*, A292-A300.

55. Lee, H.; Kim, K.; Park, Y.; An, K.; Park, S.; Kim, B. Activated carbons from thermoplastic precursors and their energy storage applications. *Nanomaterials* **2019**, *9*, 896.

56. Guo, S.; Wang, F.; Chen, H.; Ren, H.; Wang, R.; Pan, X. Preparation and performance of polyvinyl alcohol-based activated carbon as electrode material in both aqueous and organic electrolytes. *J. Solid State Electrochem.,* **2012**, *16*, 3355-3362.

57. Bello, A.; Barzegar, F.; Momodu, D.; Taghizadeh, F.; Fabiane, M.; Dangbegnon, J.; Manyala, N. Morphological characterization and impedance spectroscopy study of porous 3D carbons based on graphene foam-PVA/phenol-formaldehyde resin composite as an electrode material for supercapacitors. *RSC Adv.,* **2014**, *4*, 39066–39072.

58. Liu, M.; Yu, Y.; Liu, B.; Liu, L.; Lv, H.; Chen, A. PVP-assisted synthesis of nitrogen-doped hollow carbon spheres for supercapacitors. *J. Alloys and Compounds* **2018**, *768*, 42-48.

59. Ma, C.; Li, Z.; Li, J.; Fan, Q.; Wu, L.; Shi, J.; Song, Y. Lignin-based hierarchical porous carbon nanofiber films with superior performance in supercapacitors. *Appl. Surf. Sci.,* **2018**, *456*, 568-576.

60. Zhang, W.; Yu, C.; Chang, L.; Zhong, W.; Yang, W. Three-dimensional nitrogen-doped hierarchical porous carbon derived from cross-linked lignin derivatives for high performance supercapacitors. *Electrochim. Acta* **2018**, *282*, 642–652.

61. Tong, Y.; Li, X-M.; Xie, L-J.; Su, F-Y.; Li, J-P.; Sun, G-H.; Gao, Y-D.; Zhang, N.; Wei, Q.; Chen, C-M. Nitrogen-doped hierarchical porous carbon derived from block copolymer for supercapacitor. *Energy Storage Mater.,* **2016**, *3*, 140-148.

62. Wang, Y.; Bin Kong, L.; Li, X.; Ran, F.; Luo, Y.; Kang, L. Mesoporous carbons for supercapacitors obtained by the pyrolysis of block copolymers. *New Carbon Mater.,* **2015**, *30*, 302-309.

63. Chen, G.; Zhai, W.; Wang, Z.; Yu, J.; Wang, F.; Zhao, Y.; Li, G. Fabrication and supercapacitive properties of hierarchical porous carbon from polyacrylonitrile. *Mater. Res. Bull.,* **2015**, *72*, 204-210.

64. Yadav, N.; Promila, R.; Hashmi, S. Hierarchical porous carbon derived from eucalyptus-bark as a sustainable electrode for high-performance solid-state supercapacitors. *Sustain. Energy Fuels* **2020**, *4*, 1730-1746.

65. Demir, M.; Saraswat, S.; Gupta, R. Hierarchical nitrogen-doped porous carbon derived from lecithin for high-performance supercapacitors. *RSC Adv.,* **2017**, *7*, 42430-42442.